

JGR Space Physics

RESEARCH ARTICLE

10.1029/2019JA026521

Continent-Wide R1/R2 Current System and Ohmic Losses by Broad Dipolarization-Injection Fronts

Key Points:

- Two broad (6.5 and 4 R_E in Y_{GSM}) dipolarization-injection fronts impinged and rebounded from Earth's dipolar field lines near GEO during the same substorm
- Downward R1 and upward R2 currents grew to azimuthally cover the whole North American continent in the course of the substorm
- Regions of negative $j \cdot E'$ (generator) peaked toward the end of the impingements and were conjugate to R2 auroral current (load)

Supporting Information:

- Supporting Information S1
- Movie S1
- Movie S2

Correspondence to:

E. V. Panov,
evgeny.panov@oeaw.ac.at

Citation:





Panov, E. V., Baumjohann, W., Nakamura, R., Weygand, J. M., Giles, B. L., Russell, C. T., et al. (2019). Continent-wide R1/R2 current system and ohmic losses by broad dipolarization-injection fronts. *Journal of Geophysical Research: Space Physics*, 124, 4064–4082. <https://doi.org/10.1029/2019JA026521>

Received 18 JAN 2019

Accepted 7 MAY 2019

Accepted article online 15 MAY 2019

Published online 6 JUN 2019

E. V. Panov¹ , W. Baumjohann¹ , R. Nakamura¹ , J. M. Weygand² , B. L. Giles³ ,
C. T. Russell² , G. Reeves⁴ , and M. V. Kubyskhina⁵ 

¹Space Research Institute, Austrian Academy of Sciences, Graz, Austria, ²Institute of Geophysics and Planetary Physics, University of California, Los Angeles, CA, USA, ³NASA Goddard Space Flight Center, Greenbelt, MD, USA, ⁴Los Alamos National Laboratory, Los Alamos, NM, USA, ⁵Institute of Physics, St. Petersburg State University, St. Petersburg, Russia

Abstract We employ Magnetospheric Multiscale, Geostationary Operational Environmental and Los Alamos National Laboratory satellites, as well as the ground magnetometer networks over Greenland and North America to study a substorm on 9 August 2016 between 9 and 10 UT. We found that during the substorm two earthward flows, whose dipolarization-injection fronts exceeded 6.5 and 4 Earth's radii (R_E) in Y_{GSM} , impinged and rebounded from Earth's dipolar field lines at $L = 6-7$ downtail, where L is the McIlwain number. The impingements and rebounds ended with a substorm current system of downward R1 and upward R2 currents which grew to azimuthally cover the whole North American continent. At the fronts, regions of enhanced negative $j \cdot E'$ were formed and peaked toward the end of the impingements. These regions appeared to be conjugate with eastward moving aurora (along the growth phase arc and together with eastward drifting energetic electrons at geosynchronous equatorial orbit), which manifests ionospheric Ohmic losses.

1. Introduction

The global Region 1 (R1) and Region 2 (R2) currents close in the ionosphere through Pedersen currents forming a “Pedersen Loop” (Untiedt & Baumjohann, 1993). Such loops could be part of a meridional substorm current system (Boström, 1964; Lui & Kamide, 2003; Sugiura, 1975; Siscoe, 1982). Yang et al. (2012) performed magnetohydrodynamic simulations of a deep bubble injection in the transition region between the Earth's dipolar field lines and the stretched field lines of the Earth's magnetotail. The simulations indicated that in the background plasma sheet ahead of the bubble there is a higher-entropy structure, which is connected to the ionospheric R2 current. The lower-entropy flux tubes behind the bubble's front are connected to the ionospheric R1 current.

The transition region between the dipolar and stretched field lines is where earthward propagating dipolarization fronts stop (Dubayagin et al., 2011; Nakamura et al., 2001; Ohtani, 1998; Runov et al., 2009; Sergeev et al., 2012; Sergeev et al., 2014) and energetic particle injections are being initiated (e.g., Apatenkov et al., 2007; Baker et al., 1982; Gabrielse et al., 2014; Gkioulidou et al., 2015; Mauk & McIlwain, 1974; Lopez et al., 1990; Li et al., 1998; Reeves et al., 1990; Turner et al., 2015). Since dispersionless injections near the midnight meridian are often associated with the dipolarization front-like magnetic boundaries, they are often referred to as dipolarization-injection (DI) fronts (e.g., Moore et al., 2013; Sergeev et al., 2009). DI fronts are systematically observed to propagate near geosynchronous equatorial orbit (GEO) at velocities of 10–100 km/s (Moore et al., 1981; Reeves et al., 1996; Sergeev et al., 1998) and may intrude further inward to $L = 4$, as Van Allen probes revealed (Ohtani et al., 2018). The azimuthal size of DI fronts (Reeves et al., 1990, 1991; Thomsen et al., 2001) is similar to that of a typical bursty bulk flow (BBF; Baumjohann et al., 1990) channel, 2–3 R_E (Angelopoulos et al., 1996; Nakamura et al., 2004; Sergeev et al., 1996).

The evolution and dynamics of the DI fronts is essential for several phenomena (i) for understanding eastward electron and westward ion injections (e.g., Birm et al., 1998) and particle acceleration at the DI fronts (e.g., Birm et al., 2013; Ukhorskiy et al., 2018; Yang et al., 2011), (ii) for the plasmasphere processes, because “snowplow” DI fronts possibly ripple the plasmopause (Goldstein et al., 2005; Moore et al., 2013), and (iii) for a substorm model (e.g., Lui, 1996; Reeves et al., 1996), because a current generator region ($j \cdot E'$ would be negative for generator, cf., e.g., Cowley, 2000) and a current circuit that leads to a dissipative ionospheric load (aurora; e.g., Lui, 2004; Strangeway, 2012) are needed.

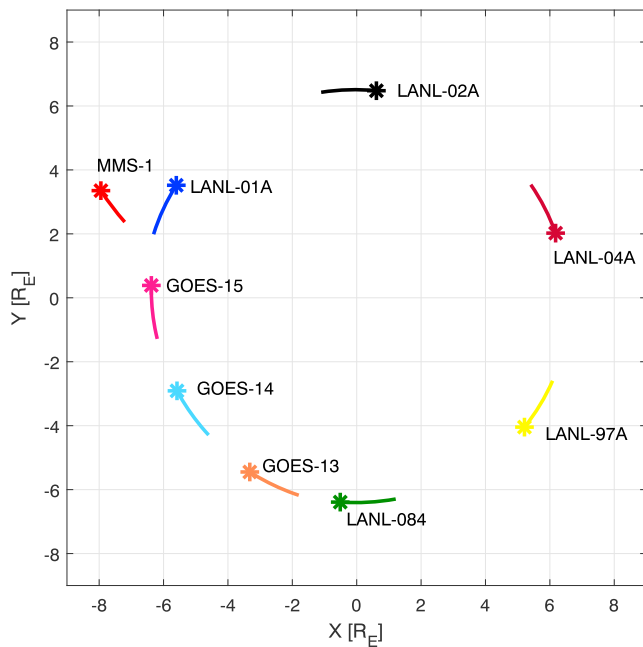


Figure 1. Orbital segments of MMS, GOES, and LANL probes in the XY GSM plane on 9 August 2016 between 09:00 (stars) and 10:00 UT. LANL = Los Alamos National Laboratory; MMS = Magnetospheric Multiscale; GOES = Geostationary Operational Environmental Satellite; GSM = Geocentric Solar Magnetospheric.

Yet ground ionospheric observations have reported on multiple onsets in the course of the same substorm (Baumjohann et al., 1981). Further in situ observations and theoretical works have suggested that intermittent BBFs creating small “wedgelets” can be responsible for multiple onsets (e.g., Birn et al., 2011; Birn & Hesse, 2014; Liu et al., 2015a; McPherron et al., 1997; Malykhin et al., 2018; Nakamura et al., 1994; Palin et al., 2016; Sergeev et al., 2000). Sparse documented proof exists on a relation between the ionospheric and plasma sheet observations, because not all BBFs can lead to global magnetotail dipolarization (Baumjohann et al., 1999) at GEO (Ohtani et al., 2006); BBFs and embedded in them DI fronts may experience tailward rebounds due to buoyancy force (Birn et al., 2011; Chen & Wolf, 1999; Nakamura et al., 2013; Panov et al., 2010; Wolf et al., 2012). Buoyancy waves caused by the rebounds (Panov et al., 2010; Panov et al., 2013b) are heavily damped and are not necessarily associated with a substorm expansion (Panov et al., 2013a, 2013; Wolf et al., 2018).

In this paper we show that two broad (6.5 and $4 R_E$ in Y_{GSM}) DI fronts impinged and rebounded from Earth’s dipolar field lines near GEO during the same substorm. In the course of the substorm, downward R1 and upward R2 currents grew to azimuthally cover the whole North American continent. The R1/R2 currents were initiated by the first DI front. The R1/R2 currents were contributed by the second DI front causing a significant local current disturbance. Regions of negative $j \cdot E'$ (generator) peaked toward the end of the impingements and were conjugate with an auroral arc (load) thus manifesting ionospheric Ohmic losses through Joule heating at the DI fronts.

GEO observations of energetic particle fluxes were provided by the National Oceanic and Atmospheric Administration’s Geostationary Operational Environmental Satellites’ (GOES) Magnetospheric Electron Detectors (Hanser, 2011) and by the Los Alamos National Laboratory (LANL) satellites’ Synchronous Orbit Particle Analyzers (Belian et al., 1992). We also used magnetic field from the GOES Space Environment Monitor Magnetometers (<https://www.ngdc.noaa.gov/stp/satellite/goes>; see also GOES N SERIES DATA BOOK, Revision D, February 2010). Magnetotail electric and magnetic field observations were provided by the four National Aeronautics and Space Administration’s Magnetospheric Multiscale (MMS) mission (Burch et al., 2016) probes’ fluxgate magnetometers and the double probe electric field instruments from the FIELDS instrument suite (Torbert et al., 2016) and the plasma observations by the Fast Plasma Instruments (Pollock et al., 2016) and Fly’s Eye Energetic Particle Spectrometers (Blake et al., 2016). Observations of the ionospheric magnetic field and auroral emissions were provided by a dense network of ground magnetometer arrays over Greenland and North America and by the All-Sky Imager (ASI) at The Pas (Mende et al., 2008; Mann et al., 2008; Weygand et al., 2011).

The outline of the paper is as follows. Section 2 shows two dawnward propagating energetic electron injections at GEO and associated two DI fronts during the substorm on 9 August 2016 between 09:00 and 10:00 UT. MMS observations of the two DI fronts and associated with them earthward flows and sequential tailward rebounds are investigated in section 3. Development of the ionospheric substorm downward R1 and upward R2 currents and auroral signatures of the DI fronts are shown in section 4. Connection of the currents that are generated at the DI fronts to the ionospheric currents is considered in section 5. Sections 6 and 7 provide discussion and conclusions.

2. Two Injections at GEO

Figure 1 shows orbital segments of MMS, GOES, and LANL probes in the XY Geocentric Solar Magnetospheric (GSM) plane on 9 August 2016 between 09:00 (stars) and 10:00 UT. The four MMS probes (MMS-1 is shown in red in Figure 1; the distances between MMS-1 and the other MMS probes were less than the line thickness) were duskward from the three GOES satellites (orange, cyan, and magenta in Figure 1) and at sim-

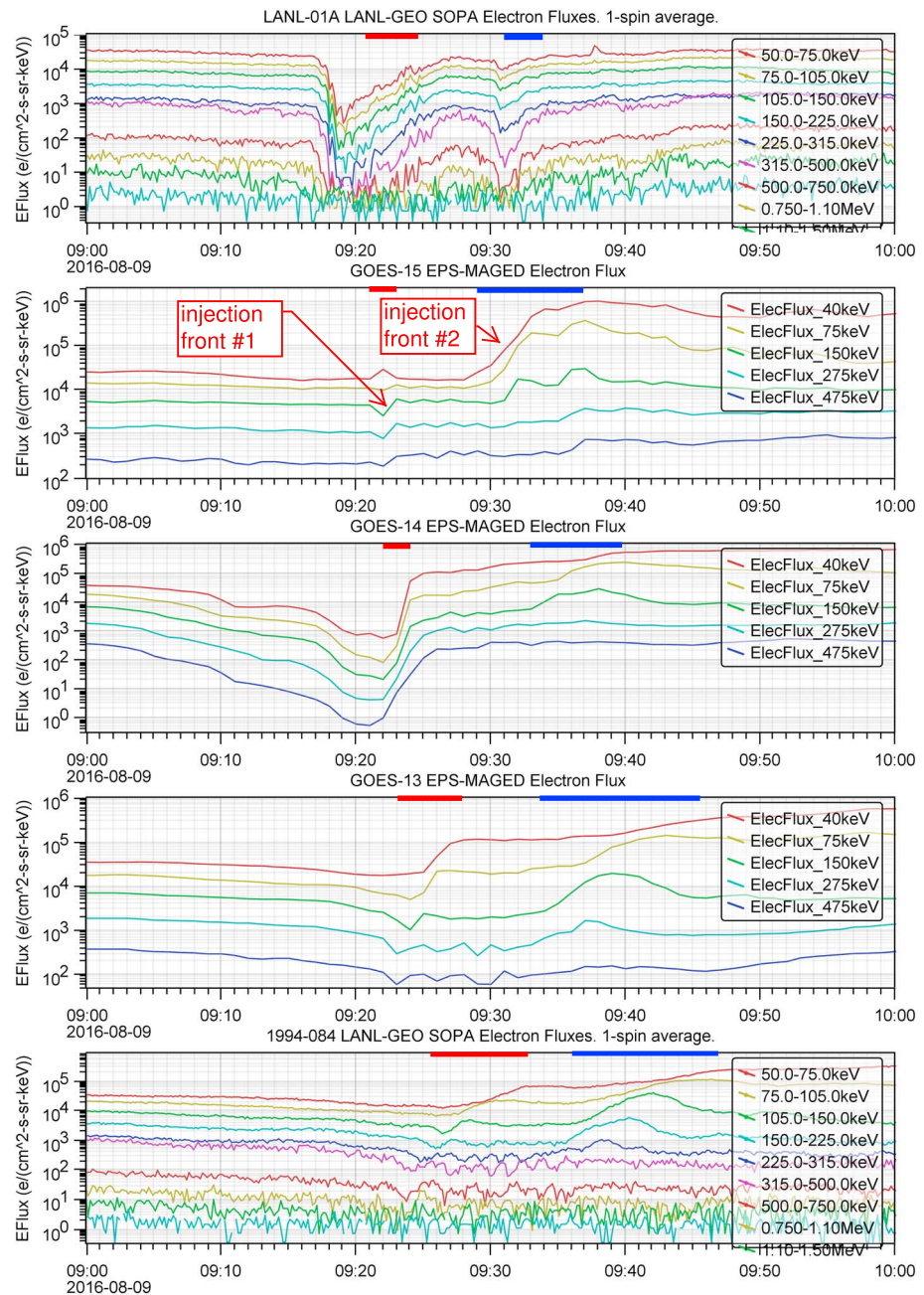


Figure 2. Downward propagation of two injection fronts as observed in GOES MAGED and LANL SOPA electron fluxes on 9 August 2016 between 09:00 and 10:00 UT. The fluxes are ordered following the GOES and LANL probes' appearance from dusk to dawn over midnight. LANL = Los Alamos National Laboratory; GEO = geosynchronous equatorial orbit; SOPA = Synchronous Orbit Particle Analyzers; GOES = Geostationary Operational Environmental Satellite; MAGED = Magnetospheric Electron Detectors; EPS = Energetic Particle Sensor.

ilar Y_{GSM} coordinates with the LANL-01A probe. LANL-1994-084 and LANL-02A were near the terminator. LANL-97A and LANL-04A were on the day side.

Figure 2 shows GOES Magnetospheric Electron Detectors and LANL Synchronous Orbit Particle Analyzers electron fluxes on 9 August 2016 between 09:00 and 10:00 UT. The fluxes are ordered following the GOES and LANL probes' appearance from dusk to dawn over midnight. Three other LANL satellites (LANL-97A, LANL-02A, and LANL-04A; cf. Figure 1) did not reveal any significant disturbances in the energetic electron fluxes and thus are not shown in Figure 2.

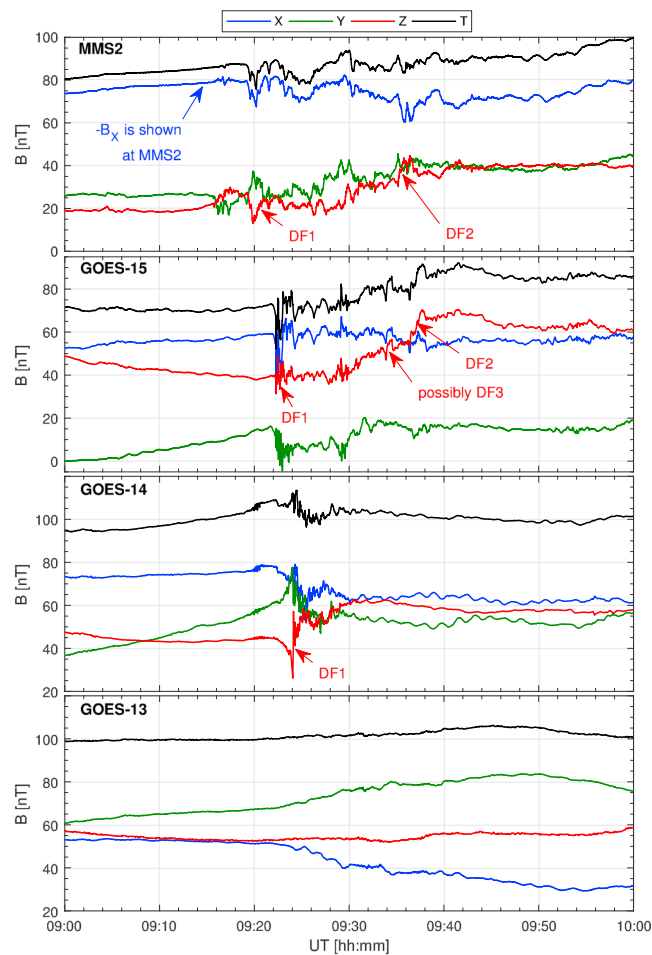


Figure 3. Three GSM components and total magnetic field from MMS-2 (first panel) and from GOES-15 (second panel), GOES-14 (third panel), and GOES-13 (fourth panel) on 9 August 2016 between 09:00 and 10:00 UT. See legend for color coding. MMS = Magnetospheric Multiscale; GOES = Geostationary Operational Environmental Satellite; GSM = Geocentric Solar Magnetospheric.

Two different injections of energetic electrons were observed in the energetic electron data. The horizontal bars in each panel in Figure 2 highlight the appearance of two injection fronts by the five probes (red bars for injection front #1 and blue bars for injection front #2). The first injection was detected by all the presented satellites between 9:20 and 9:30 UT. This injection was nearly dispersionless at LANL-01A, GOES-15, and GOES-14. GOES-15 observed the injection only slightly (1–2 min) earlier than the two other probes (at 9:22 UT). In contrast, GOES-13 and later LANL-1994-084 observed dispersive injections.

The second injection was observed by the five probes at GEO between 9:33 and 9:45 UT. In contrast to the first injection, the second injection was dispersive at GOES-14 between 9:33 and 9:37 UT. Later (between 9:36 and 9:45 UT), the second dispersive injection was observed at GOES-13 and LANL-1994-084 probes. The second injection was dispersed broader in time than the first injection (cf. GOES-13 and LANL-1994-084 data).

Figure 3 shows three GSM components and the total magnetic field from MMS-2 (first panel), GOES-15 (second panel), GOES-14 (third panel), and GOES-13 (bottom panel) for the same time interval as in Figure 2. GOES-15 observed two dipolarization fronts around the onset times of two injection fronts shown in Figure 2. The first dipolarization front was clearly seen at MMS and GOES-14 (highlighted by the red text arrow “DF 1” in Figure 3). The dipolarization front during the second injection front was observed at MMS but did not show up at GOES-14 (highlighted by the red text arrow “DF 2” in Figure 3). None of the two dipolarization fronts was observed by GOES-13. Throughout the paper, we use the term DI front when

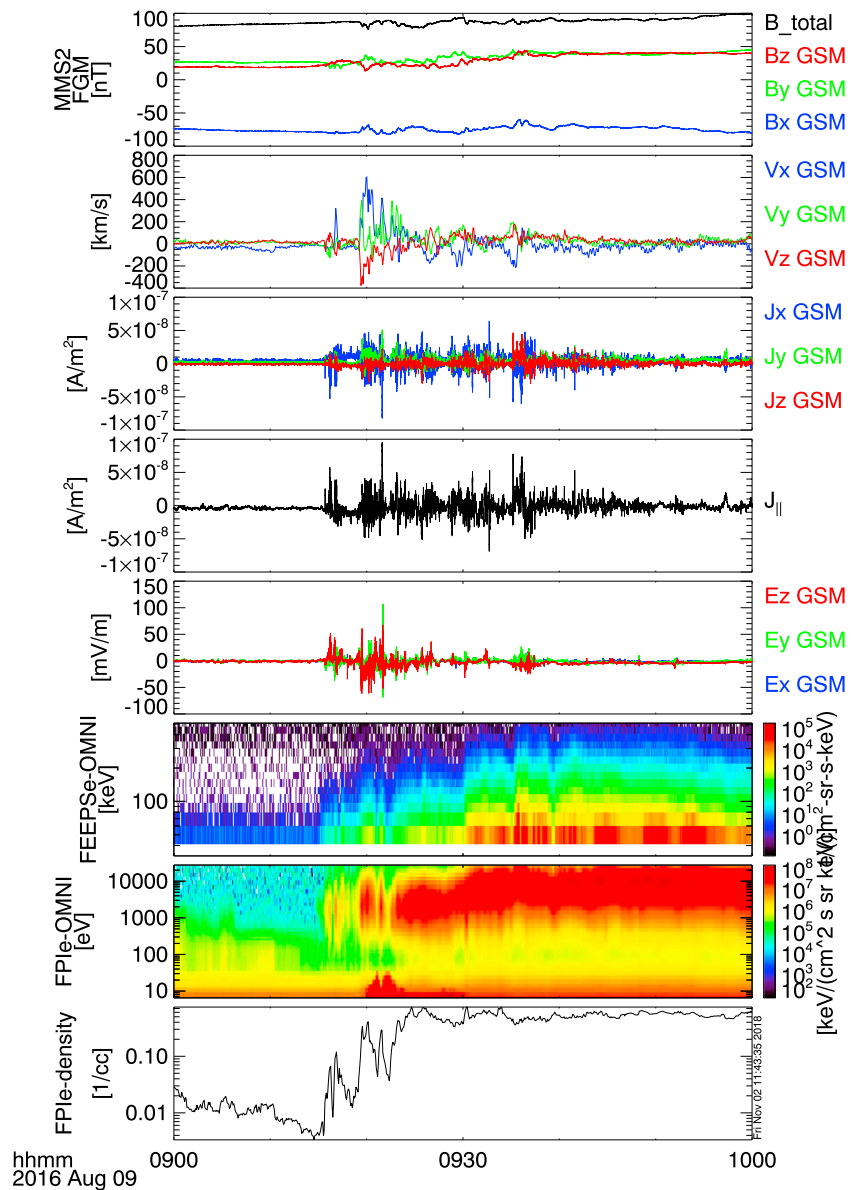


Figure 4. MMS-2 data on 9 August 2016 between 09:00 and 10:00 UT. From top to bottom at survey cadence are shown: GSM components of the magnetic field, the ion velocity, and the current density, the parallel component of the current density, GSM components of the electric field, FEEPS and FPI electron spectrograms, and FPI electron density. MMS = Magnetospheric Multiscale; FEEP = Fly’s Eye Energetic Particle Spectrometer; FPI = Fast Plasma Instrument; GSM = Geocentric Solar Magnetospheric; FGM = Flux Gate Magnetometer; OMNI = Omnidirectional.

there exists a sharp boundary in the magnetic field that is associated with a dispersionless energetic particle injection.

3. Earthward Flows and Tailward Rebounds

Figure 4 shows MMS-2 probe data for the same time interval as the top panel in Figure 3. Around 9:20 UT, the magnetic field components (top panel in Figure 4) exhibited signatures of a dipolarization front that was embedded in an earthward flow with the peak velocities of about 600 km/s (second panel in Figure 4). With the arrival of the flow, the local plasma sheet currents appeared to be enhanced and modulated till about 9:50 UT (third and fourth panels in Figure 4). The dipolarization front around 9:20 UT was also associated with energetic electrons with energies up to few hundred kiloelectron volts (sixth and seventh panels in Figure 4). One can notice another clear injection of the energetic electrons around 9:36 UT, which was

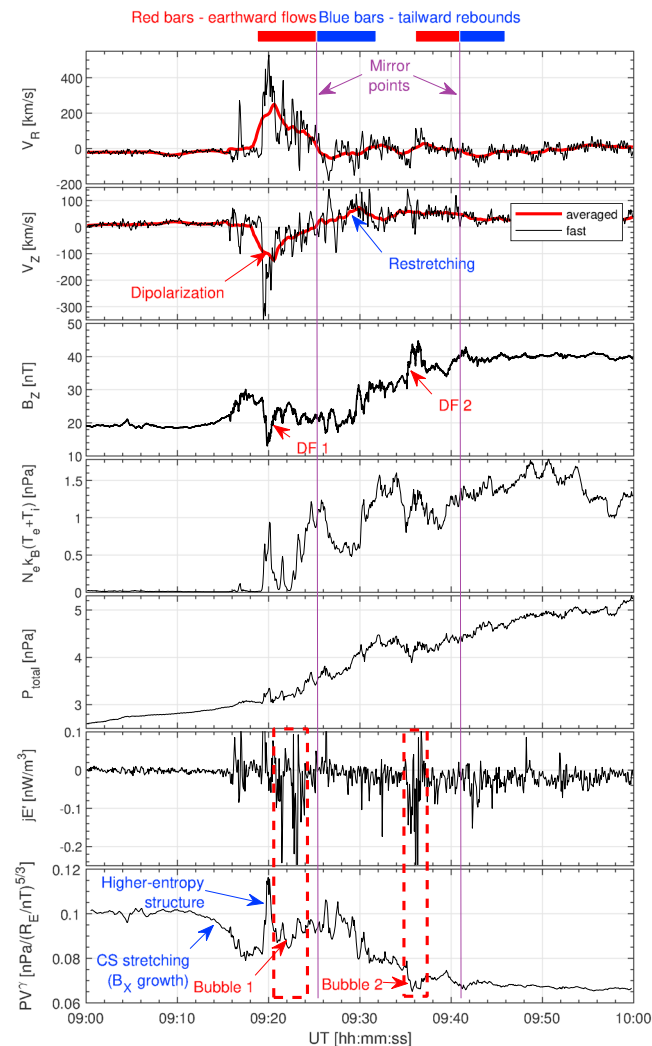


Figure 5. Magnetospheric Multiscale-2 data on 9 August 2016 between 09:00 and 10:00 UT. From top to bottom at survey cadence are shown: Radial (V_R ; calculated from V_X and V_Y with positive values toward Earth) and Z-GSM velocity components together with their sliding window averages (red), X-GSM magnetic field component, FPI particle pressure (sum of the electron and ion pressures), sum of the magnetic pressure and the FPI particle pressure, scalar product of the current density (calculated from the curl of the magnetic field), and the electric field in the plasma frame, local flux tube entropy $PV^{5/3}$.

associated with a burst of strongly enhanced energetic electron fluxes. A significant burst in the parallel current can clearly be seen around the same time (panel four in Figure 4). That is, both injections that were seen at GEO (Figures 2 and 3) were also observed by the MMS probes in the plasma sheet between $7 R_E$ and $8 R_E$ downtail.

Before 09:25:30 UT the radial ion velocity V_R (calculated from V_X and V_Y with positive values toward Earth) was largely earthward (top panel in Figure 5). Then, around 09:25:30 UT V_R turned tailward and kept this direction till about 09:31 UT. The earthward and tailward V_R is highlighted by the red and blue bars around 09:25:30 UT in the top of Figure 5. Such change of sign in V_R could mean a flow rebound when interacting with the Earth's dipolar field lines (cf. Figure 2 in Panov et al., 2010, for a rebound example; e.g., THEMIS probe P3 data). Among the rebound signatures would be bipolar variations in V_Z and B_X that manifest dipolarization or stretching of the plasma sheet around the rebound time (cf. Figure 3 in Panov et al., 2010). Indeed, bipolar variations in V_Z and B_X were identified in the MMS data (highlighted by the red and blue text arrows in Figure 5; for B_X cf. the top panel in Figure 3 between 9:23 and 9:28 UT). We separate the earthward flow from the tailward rebound by the vertical magenta line at 09:25:30 UT in Figure 5 and name this “mirror point.” Another earthward flow and tailward rebound that were seen in V_R and B_X were observed by MMS

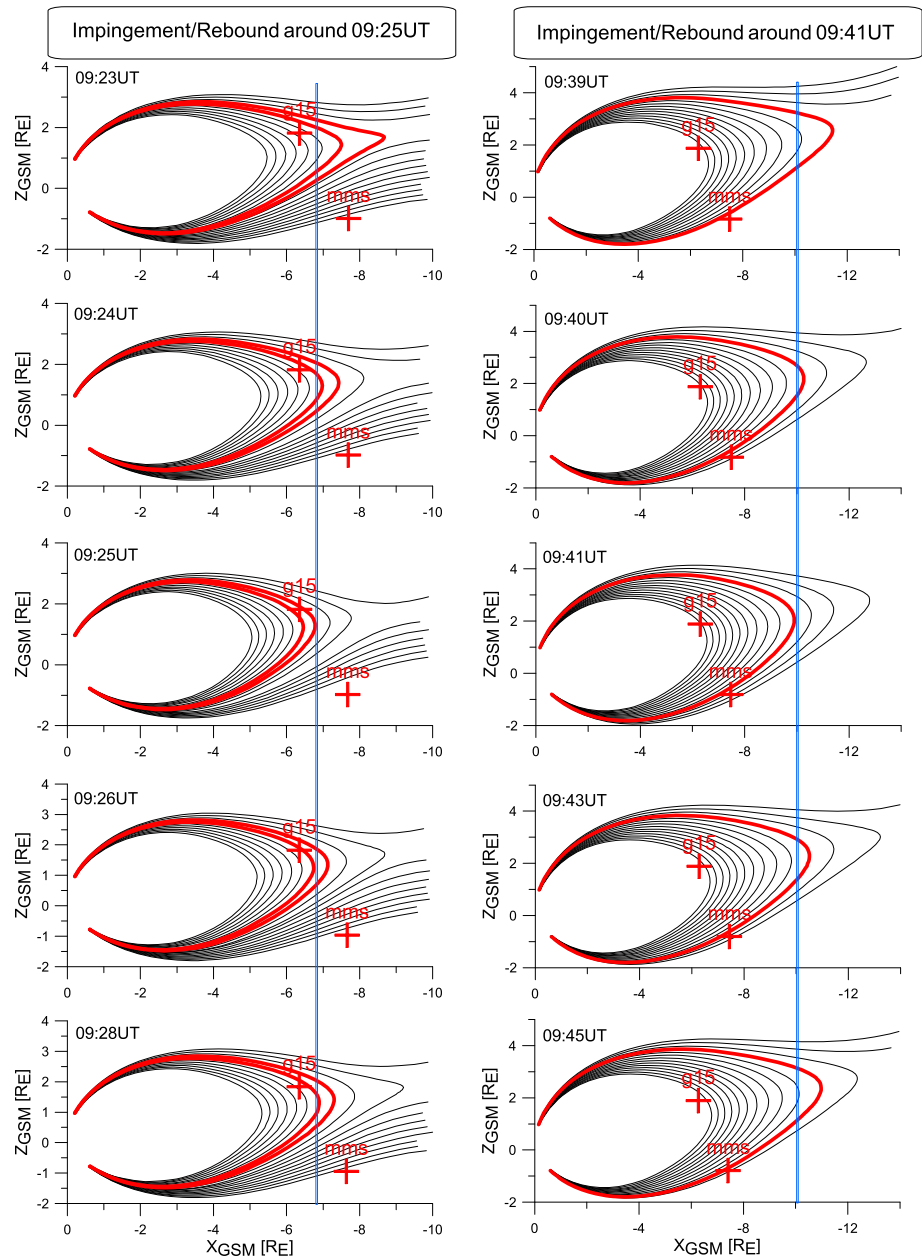


Figure 6. Locations of Geostationary Operational Environmental Satellite-15 and MMS probes on 9 August 2016 between 09:23 and 09:28 UT (left column) and between 09:39 and 09:45 UT (right column) projected onto the MMS meridian GSM plane, and evolution of the magnetic field lines. MMS = Magnetospheric Multiscale; GSM = Geocentric Solar Magnetospheric.

around 09:41 UT and are also highlighted by the other red and blue rectangles (the variations in V_z during the second rebound were not as clear as during the first rebound).

The sum of the magnetic and the particle pressures P_{total} at MMS-2 (fifth panel in Figure 5) increased from one quasi-asymptotic value (2.6 nPa) at 09:00 UT to another quasi-asymptotic value (about 5 nPa) at 10:00 UT. The scalar product of the current density, which was calculated from the curl of the magnetic field, and the electric field in the plasma (electron) frame $\mathbf{j} \cdot \mathbf{E}'$ was around zero between 09:00 and 09:16 UT. After 09:16 UT $\mathbf{j} \cdot \mathbf{E}'$ was negative at about -0.01 nW/m^3 on average. At two occasions (around 09:23 and 09:36 UT), $\mathbf{j} \cdot \mathbf{E}'$ exhibited strongly negative peaks with the peak values exceeding -0.2 nW/m^3 . The appearance of the two negative peaks in $\mathbf{j} \cdot \mathbf{E}'$ (highlighted by two red dashed rectangles in Figure 5) coincided with the appearance of the two DI fronts in Figures 2 and 3. The appearance of the two negative peaks in $\mathbf{j} \cdot \mathbf{E}'$ in

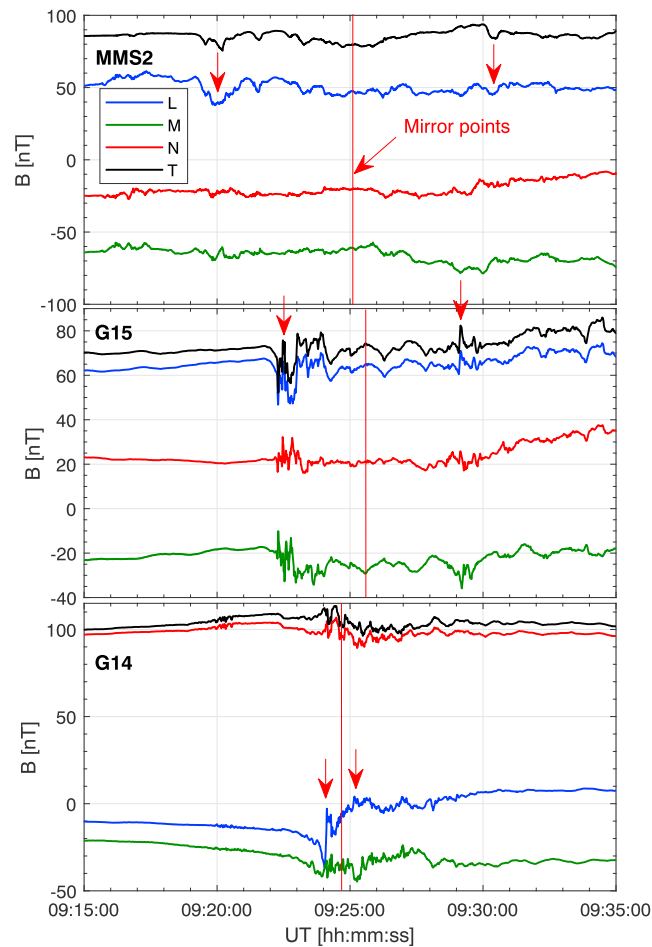


Figure 7. Minimum variance components (see text for minimum variance coordinates definition) and total magnetic field from MMS-2 (top) and from Geostationary Operational Environmental Satellite-15 (middle) and Geostationary Operational Environmental Satellite-14 (bottom) on 9 August 2016 between 09:15 and 09:35 UT. See legend for color coding. MMS = Magnetospheric Multiscale.

Figure 5 occurred toward the end of the earthward V_R . The bottom panel in Figure 5 shows the local flux tube entropy $PV^{5/3}$, for which the flux tube volume V was calculated using formula (6) in Wolf et al. (2006). The local entropy gradually decreased before 9:17 UT (together with B_x growth) as a result of the magnetotail current sheet stretching before substorm expansion. The two negative peaks in $j \cdot E'$ coincided with decreases in $PV^{5/3}$, which can be interpreted as bubbles (denoted as “Bubble 1” and “Bubble 2” in the bottom panel of Figure 5). There also exist a higher entropy structure ahead of Bubble 1 at 9:20 UT (cf. the blue text arrows in the bottom panel in Figure 5).

Figure 6 shows locations of GOES-15 and MMS probes projected onto the MMS meridian GSM plane and the evolution of the magnetic field lines predicted by the AM-03 version of the adapted model (Kubyskhina et al., 2011) on 9 August 2016 between 09:23 and 09:28 UT (left) and between 09:39 and 09:45 UT (right). The two time periods were chosen around the two mirror points indicated by two vertical magenta lines in Figure 5. All five snapshots in the two columns in Figure 6 show the same set of the magnetic field lines. Selected (same) field lines are shown in bold red. According to the AM-03 model, magnetic field line evolution shows that the magnetotail dipolarized during the earthward flows, which were observed before the mirror points. The magnetotail restretched during the tailward rebounds, which were observed after the two mirror points. The most earthward positions that were reached by the bold red field lines are indicated by two vertical blue lines in Figure 6.

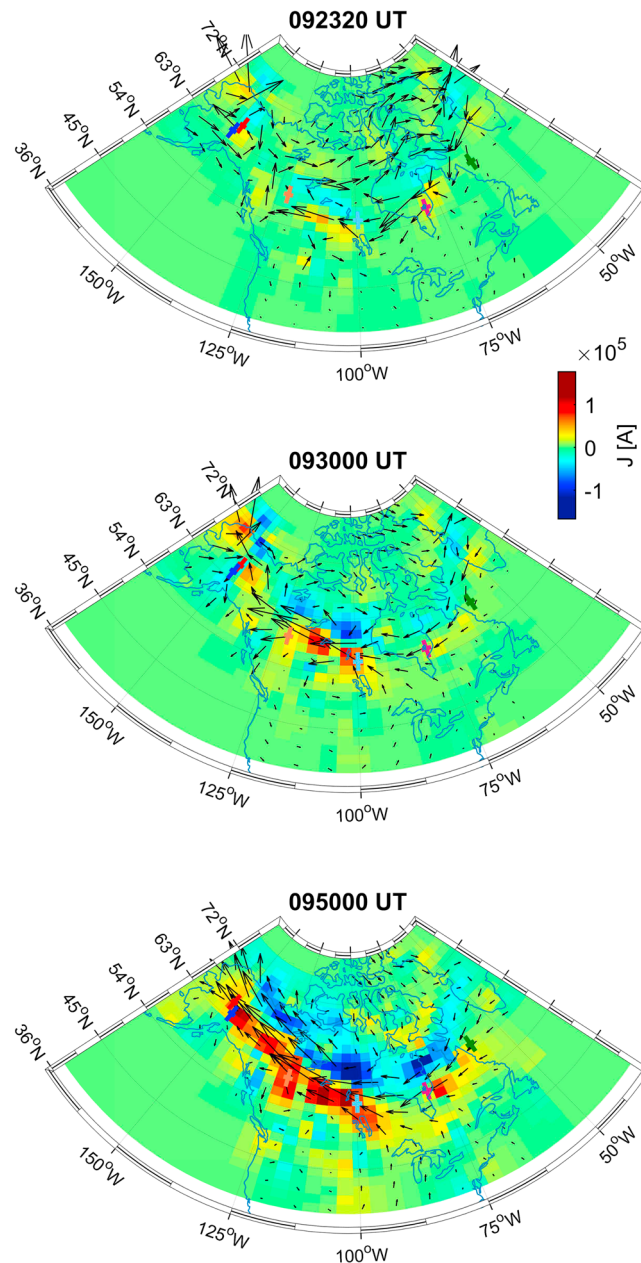


Figure 8. Ionospheric currents: snapshot of equivalent ionospheric currents (arrows) and the Spherical Elementary Current System current amplitudes (color: upward in reddish and downward in bluish) on 9 August 2016 at 9:23:20 UT (top), 9:30:00 UT (middle), and 9:50:00 UT (bottom), calculated using ground-based magnetometer array data. The footprints of the MMS-2, Geostationary Operational Environmental Satellite (GOES)-13 through GOES-15, LANL-01A, and LANL-084 are overplotted by crosses as predicted by the Tsyganenko 96 model (red for MMS-2, orange for GOES-15, cyan for GOES-14, magenta for GOES-13, blue for LANL-01A, and green for LANL-084). MMS = Magnetospheric Multiscale; GOES = Geostationary Operational Environmental Satellite; LANL = Los Alamos National Laboratory.

Figure 7 shows the total and three minimum variance magnetic field components from MMS-2 (top), from GOES-15 (middle), and GOES-14 (bottom) on 9 August 2016 between 09:15 and 09:35 UT. The minimum variance coordinates were identified across the dipolarization fronts that were observed around 9:20 UT by MMS-2, around 9:22:30 UT by GOES-15, and around 9:24 UT by GOES-14. The corresponding normal directions were mainly in the XZ GSM plane for all three probes ($n_{\text{MMS}2} = [0.64, -0.12, 0.76]$, $n_{\text{G}15} = [0.21, -0.26, 0.94]$, $n_{\text{G}14} = [0.84, -0.25, 0.48]$). The significant Z component in the three normals is probably because all three probes were far from the neutral sheet. Assuming that the DI front still existed in

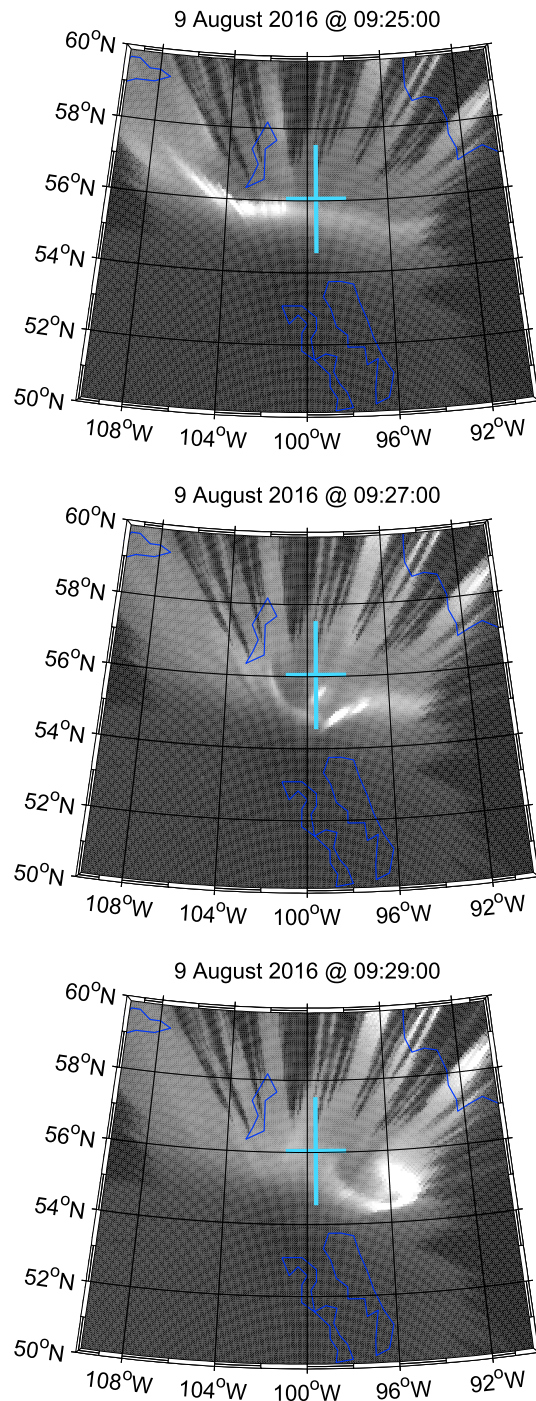


Figure 9. Snapshots of All-Sky Imager observations of auroral activity at The Pas on 9 August 2016 at 9:25:00 UT (top), 09:27:00 UT (middle), and at 9:29:00 UT (bottom). The footprints of Geostationary Operational Environmental Satellite-14 predicted by the Tsyganenko 96 model are overlotted (cyan crosses).

the tailward rebound flow, one could identify the remnants of the DI front that were passing the three probes during the tailward rebound (i.e., after 09:25 UT). The red arrows in Figure 7 before the vertical red lines (mirror points) indicate the crossings of the dipolarization front before the flow rebound. The red arrows in Figure 7 after the vertical red lines indicate the assumed remnants of the dipolarization fronts during the fronts' rollback with the flow tailward rebound. Indeed, the dipolarization front structure in the incident flow exhibited significant similarities with the highlighted magnetic structures during the rollback.

4. Ionospheric Substorm Current System

We used magnetometer arrays over Greenland and North America (Mende et al., 2008; Mann et al., 2008; Weygand et al., 2011) and the 2-D Spherical Elementary Current Systems (SECSs) method (Amm & Kauristie, 2002; Weygand et al., 2011) to investigate ionospheric currents on the ground. In this method, the divergence-free elementary current system is expanded at each pole of the grid shown in Figure 2 of Weygand et al. (2011), allowing derivation of horizontal equivalent ionospheric currents (EICs). Using EICs, we calculated vertical components of the curl of EICs integrated over each grid point area. We refer to the vertical components as SECS current amplitudes (scaling factors) because the amplitude of each elementary system is scaled (measured in amperes). Under assumption that the gradient in the ionospheric conductance perpendicular to the electric field is zero, the SECS current amplitudes are expected to be proportional to field-aligned currents (FACs; Amm & Kauristie, 2002). The factor of proportionality between FACs and the SECS current amplitudes is the Hall-to-Pedersen conductance ratio.

Figure 8 shows snapshot of EICs (arrows) and SECS current amplitudes (color: upward, reddish; downward, bluish) at 9:23:20 UT (top), 9:30:00 UT (middle), and 9:50:00 UT (bottom; see movie containing all snapshots for 9 August 2016 between 9:00 and 10:00 UT at 1-s cadence in the supporting information). The footprints of the MMS-2, GOES-13 to GOES-15, LANL-01A, and LANL-084 probes as predicted by the Tsyganenko 96 model are denoted by overplotted crosses (cf. caption of Figure 8 for color coding).

The substorm current system on the ground started to be formed around 9:23:20 UT, when small upward and downward current spots appeared between GOES-15 and GOES-14 footprints (top snapshot in Figure 8). The current system consists of a pair of vertical (FAC) currents with opposite polarity (reddish and bluish spots in the SECS current amplitudes) and a westward electrojet (larger arrows in EICs between the reddish and bluish spots). After 9:23:30 UT the area of the enhanced upward and downward ionospheric currents drastically expanded in both the azimuthal and meridional directions (middle snapshot in Figure 8).

The calculated SECS current amplitudes are in agreement with the plots provided by the Active Magnetosphere and Planetary Electrodynamics Response Experiment (AMPERE; <http://ampere.jhuapl.edu/products/plots/index.html>), which confirmed the growing across the North America downward R1 and upward R2 currents eastward of the Harang discontinuity in the course of the substorm. The AMPERE currents have a much lower time resolution (once in 2 min) and thus are not shown here. By 9:50 UT the substorm current system downward R1 and upward R2 currents grew to azimuthally cover the whole North American continent (bottom snapshot in Figure 8).

On 9 August 2016 between 9:00 and 10:00 UT THEMIS ASI observations were largely under cloudy skies except for the ASI at The Pas between 9:00 and 9:38 UT. The zenith of the ASI at The Pas was near the footprint of GOES-14. Figure 9 shows snapshots of ASI observations of auroral activity at The Pas on 9 August 2016 at 9:25:00 UT (top), 09:27:00 UT (middle), and at 9:29:00 UT (bottom). The footprints of GOES-14 predicted by the Tsyganenko 96 model are overplotted (cyan crosses). A movie (in the supporting information) containing all ASI snapshots on 9 August 2016 between 9:00 and 9:38 UT at 3-s cadence shows the auroral dynamics. The footprint of GOES-14 appeared to be located at the growth phase arc. A sudden brightening of the growth phase arc appeared to start on the western (left) side from the field of view of the ASI at The Pas (top snapshot in Figure 9). Around 9:27 UT the brightening passed by the footprint of GOES-14 and went further eastward along the former growth phase arc (middle and bottom snapshots in Figure 9).

5. Plasma Sheet-Ionosphere Current Circuit

The three upper panels in Figure 10 show the auroral electrojet AE index, the total luminosity within the field of view of the All-Sky Imager at The Pas, and the total upward and downward SECS current amplitudes summed over the area between 38°N and 75°N geographic latitude and 55–145°W geographic longitude on 9 August 2016 between 09:00 and 10:00 UT. The parallel SECS current amplitudes repeated the major behavior of the AE index. The sharp growth in the total luminosity at The Pas coincided with the onset in the SECS current amplitudes growth. Two further panels in Figure 10 show that the plasma sheet parallel current density component calculated using magnetic field from the four MMS probes and disturbances in the total magnetic field as observed by MMS and GOES-14 to GOES-15 started up to 5 min before the ionospheric current growth onset.

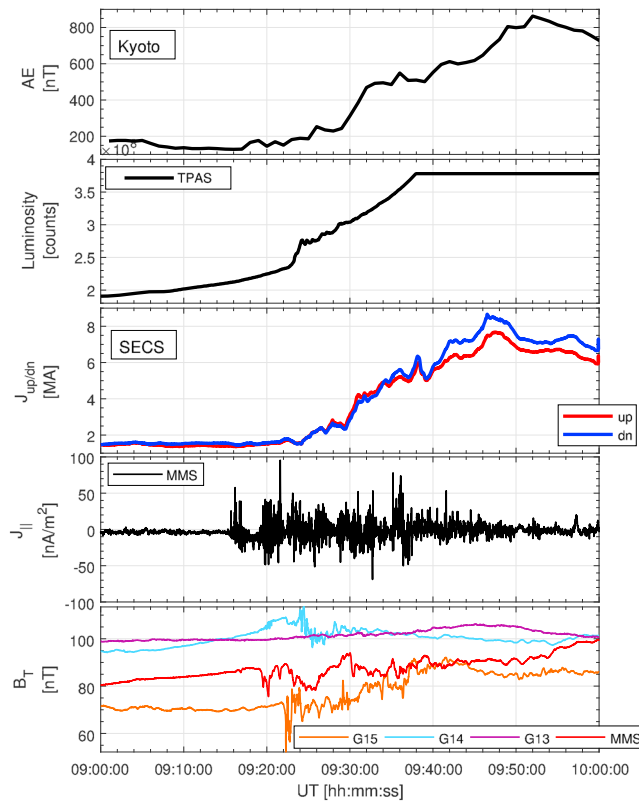


Figure 10. Ground, geostationary, and plasma sheet observations on 9 August 2016 between 09:00 and 10:00 UT (from top to bottom): Auroral electrojet (AE) index, total luminosity at The Pas, total upward and downward SECS current amplitudes summed over the area between 38°N and 75°N geographic latitude and 55–145°W geographic longitude, parallel current density component calculated using magnetic field from the four MMS probes and the total magnetic field as observed by MMS-2 and Geostationary Operational Environmental Satellite-13 to Geostationary Operational Environmental Satellite-15 probes. SECS = Spherical Elementary Current System; MMS = Magnetospheric Multiscale; TPAS = The Pas, MB, Canada.

Based on significant similarities of the profiles of the magnetic field and the current density components at different probes and in SECS current amplitudes, one could identify specific time delays of signal propagation between different locations in space and in the ionosphere. Figures 11 and 12 show ionospheric (upward SECS current amplitudes, top panels in Figures 11 and 12), geosynchronous (GOES-15, second panels in Figures 11 and 12), and plasma sheet (MMS-2, panels 3–7 in Figures 11 and 12) data during the two earthward flows with the embedded dipolarization fronts (highlighted in Figures 5 and 3). The upward SECS current amplitudes and GOES-15 data in Figures 11 and 12 were shifted backward relative to the MMS-2 data. The corresponding time shifts for the upward SECS current amplitudes and for the total magnetic field component at GOES-15 are given in the panel captions.

Further panels in Figures 11 and 12 reveal similarities for two dipolarization fronts in the V_x GSM component of the ion velocity, in GSM components of the magnetic field, in the parallel current density component, and in the scalar product of the current density (calculated from curl of the magnetic field) and of the electric field in the plasma (electrons) frame. Both dipolarization fronts are associated with local maxima in the SECS current amplitudes, with first drops and then increases in the total field at GOES-15, with growing V_{Xi} , with bursts of enhanced parallel currents and with negative $j \cdot E'$. The total magnetic field B_T at GOES-15 was defined by B_x between 9:16 and 9:26 UT and by B_z between 9:34 and 9:38 UT. B_T at GOES-15 almost repeated the shape of B_x at MMS (cf. e.g., similar minima in the GOES-15 B_T and in MMS B_x at 9:19:30, at 9:20:10, at 9:21:35, and at 9:23:15 UT). Similar variations of B_x at GOES-15 and MMS can also be seen in Figure 12 (cf., e.g., similar minimum in the GOES-15 B_T and in MMS B_x before DF 2 at 9:35:07 UT and a rapid drop in the GOES-15 B_T and in MMS B_x after DF 2 between 9:36:30 and 9:37:00 UT). B_y and B_z components before DF 1 in Figure 11 and before DF 2 in Figure 12 were anticorrelated around the B_T dips at 9:20:10 and 9:35:07 UT. The negative peaks in $j \cdot E'$ corresponded to local positive maxima in the paral-

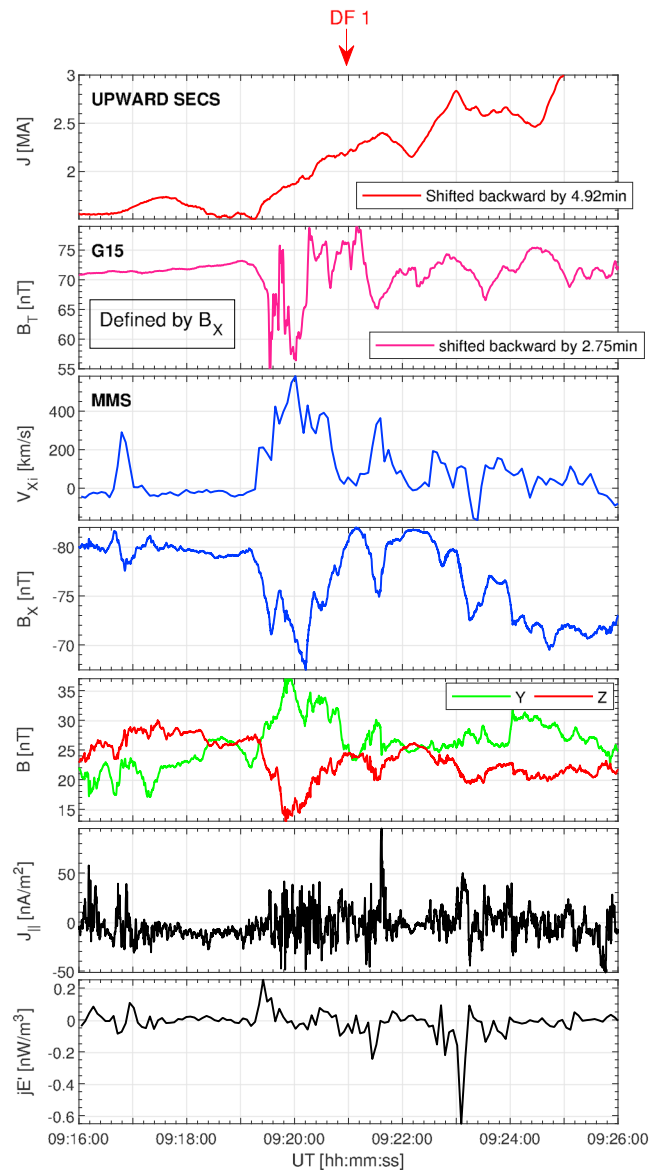


Figure 11. Ground, geostationary, and plasma sheet observations of the dipolarization-injection front on 9 August 2016 between 09:16 and 09:26 UT (DF 1 in Figure 5; from top to bottom): total upward SECS current amplitudes from Figure 10, total magnetic field from Geostationary Operational Environmental Satellite-15, V_X GSM component of the ion velocity, GSM components of the magnetic field, parallel current density component calculated using magnetic field from the four MMS probes, and scalar product of the current density (calculated from curl of the magnetic field) and of the electric field in the plasma frame. Data in the two upper panels were shifted back in time to account for the propagation time delays (see legends for delay estimates). SECS = Spherical Elementary Current System; MMS = Magnetospheric Multiscale; GSM = Geocentric Solar Magnetospheric.

parallel current observed by the four MMS probes and in the SECS current amplitudes. Because MMS was in the Southern Hemisphere, positive parallel currents at MMS corresponded to the upward ionospheric currents in the Southern Hemisphere. The time delay between GOES-15 and MMS for the dipolarization front around 9:20 UT was about 2.75 min, which is 2.2 times longer than for the dipolarization front around 9:35 UT (about 1.25 min). That is, the dipolarization front around 9:35 UT moved more than 2 times faster from MMS to GOES-15 than the dipolarization front around 9:20 UT. Based on the found time delays, we conclude that major magnetic field disturbances due to DI fronts were first observed by MMS and then the disturbances propagated to GEO and down to the ionosphere.

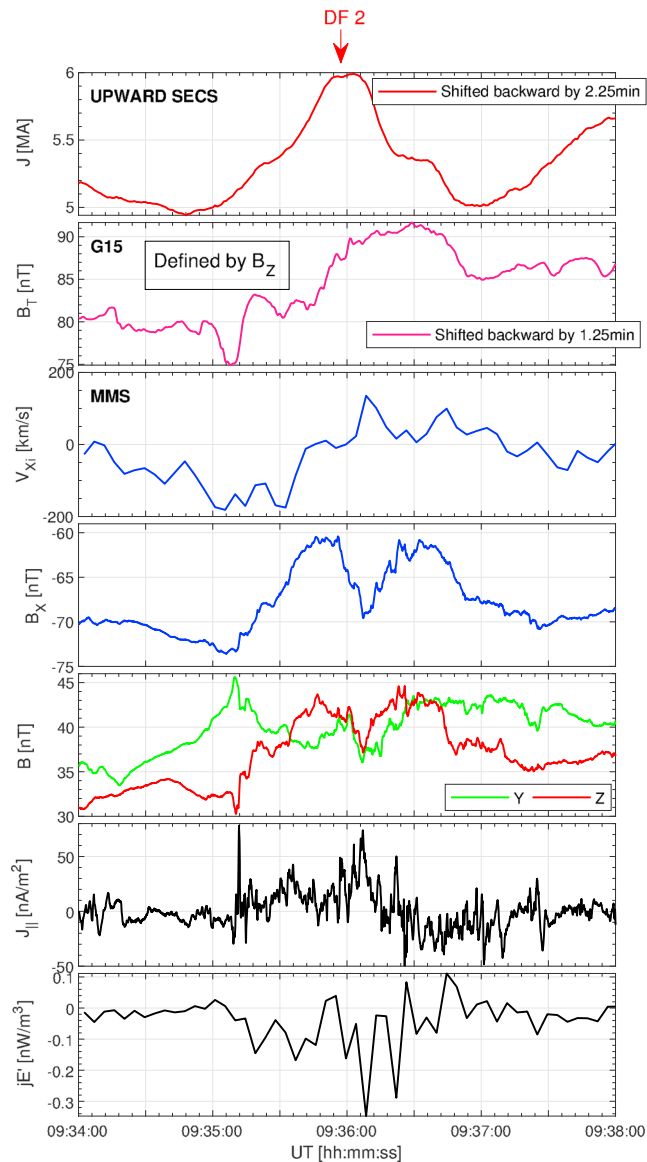


Figure 12. Same as in Figure 11 for the dipolarization-injection front on 9 August 2016 between 09:34 and 09:38 UT (DF 2 in Figure 5).

6. Discussion

The analysis revealed that the parallel current was generated at the DI fronts around 9:20 UT and around 9:35 UT, causing enhancements in the upward and downward SECS current amplitudes in the ionosphere. The conjugate ASI observations at The Pas revealed that the dipolarization front around 9:20 UT was conjugate with the auroral arc that acted as load (Figure 9). The second DI was seen by GOES-15 but never made it to GOES-14, which is probably the reason why the ASI at The Pas did not observe any auroral intensification during DF 2.

For the substorm under study ($AE \approx 800$ nT) we clearly identified two DI fronts. Whereas the ground R1/R2 currents were initiated by the first DI front, the R1/R2 currents were contributed by the second DI front causing a significant local ionospheric current disturbance. Previous observations showed that injections vary in size and in the level of energization (e.g., Gabrielse et al., 2014; Gkioulidou et al., 2015). Smaller injections could have been missed in the energetic particle measurements either because of insufficient time resolution of the particle instruments at GEO or because smaller injections were made by particles with the energies lower than the range of the particle detectors at GEO. Indications of (both temporally and spatially)

smaller injection fronts are present, for instance, in the energetic electron data from GOES-15 (second panel in Figure 2), where the electrons with energies 75–150 keV exhibited two peaks during injection front #2. It may well be that the first of the two peaks (around 9:34 UT) is due to a smaller dipolarization front that was observed by GOES-15 only (denoted by the text arrow “possibly DF3” in the second panel in Figure 3). Other dipolarization fronts that did not reach GEO (experienced rebounds tailward) but contributed to the ground R1/R2 currents were possibly also missed in this study.

The injection front #1 (red bars in Figure 2) appeared to be dispersed at GOES-13 and at LANL-1994-084. The injection front #2 (blue bars in Figure 2) appeared to be dispersed also at GOES-14. Neither GOES-13 during both injection fronts nor GOES-14 during the injection front #2 revealed any magnetic signatures of a dipolarization front (two lower panels in Figure 3). In contrast, the two injections were dispersionless at MMS, LANL-01A, GOES-15, and GOES-14 (only injection front #1) and exhibited a sharp boundary in the magnetic field (there were no magnetometers at LANL satellites). The dispersive electron injections are solely due to azimuthal energetic electron drift and not due to propagation of the dipolarization fronts. Smaller time delay (1.25 min) between the MMS and GOES-15 data for the DI front at 9:36 UT in Figure 12 than the 2.75-min delay for the DI front at 9:21 UT in Figure 11 indicates that the DI front at 9:36 UT moved earthward about 2.2 times faster than the DI front at 9:21 UT. At the same time, the energetic electron fluxes at GOES-13 and LANL-1994-084 in Figure 2 exhibited broader dispersion of the second injection. This fact is in agreement with the idea that a faster moving DI front provides stronger particle acceleration (e.g., Birn et al., 2013).

The observations of bounced off DI fronts are not unique. THEMIS probe P3 data in Figure 2 in Panov et al. (2010) during a similar (although much shorter, about 3 min long) rebound reveals a similar bounced off dipolarization front around 09:14:02 UT on 17 March 2007. Also, the bottom part of Figure 10 in Nakamura et al. (2013), which is plotted in similar format as Figure 7, revealed both the incident (denoted as IV) and probably bounced off (denoted as V) dipolarization fronts as seen by Cluster 1 on 7 September 2007 between 12:52:30 and 12:54:00 UT. The authors of the two studies did not consider that pairs of dipolarization fronts could be the same fronts before and after BBF rebounds.

The azimuthal extensions of DI fronts in Figures 11 and 12 were significantly larger than the typical dipolarization front width at GEO (about $3 R_E$ according to Figure 3 in Liu et al., 2015b). This might be the reason for the azimuthally large substorm current system in the ionosphere (present Figure 8). Since the width of dipolarization fronts may be related to the maximum ion outflow speed in the reconnection jet (Arnold et al., 2018), the azimuthal size of the corresponding ionospheric current system may also depend on the reconnection jet speed. Reconnection jets with different speed (or alternatively dipolarization fronts with different width) could lead and contribute to pseudo-breakups and small or global substorms (Miyashita et al., 2018; Nakamura et al., 1994).

Plasma sheet dipolarization (thinning) earthward of DI fronts and plasma sheet thinning (dipolarization) tailward of DI fronts occur simultaneously before (after) BBF rebounds (Nakamura et al., 1994; Panov et al., 2010). This is expected to lead to local and temporal collapse of the magnetic field lines in the transition region between the dipolarizing and stretching field lines, with the strongest field line tension at the time of the BBF stopping. This region can be identified in the MMS, GOES-15, and GOES-14 data as B_{total} maxima around 9:21 and 9:36 UT in Figures 11 and 12. According to Figures 11 and 12, MMS observed the largest negative $j \cdot E'$ at the B_{total} maxima around 9:21 and 9:36 UT (see also two red dashed rectangles in Figure 5). Thus, $j \cdot E'$ was significantly negative toward the end of the two earthward flows. In contrast, $j \cdot E'$ was much weaker during the two tailward rebounds. This is in agreement with the idea that the significant stresses were formed when the BBFs reached their most earthward (stopping) point. Since the stresses relaxed during the two tailward rebounds, an appearance of strong negative $j \cdot E'$ may be indicative for newly arriving BBFs.

As global dipolarization progressed, the average local entropy decreased (cf. the bottom panel in Figure 5). This fact is in agreement with the arrival of Bubble 2, which has lower entropy than Bubble 1 (e.g., Chen, 2016). The magnetohydrodynamic simulations of a deep bubble (Yang et al., 2012) and theoretical considerations (e.g., Chen, 2016) predict azimuthal spreading and reducing radial extension of a bubble before stopping. The simulated parallel currents suggest that the arc at The Pas is supposed to be located on the eastward side of the ionospheric projection of the bubble (cf. Figures 6 and 11 in Yang et al., 2012). The ASI at White Horse, which was located few degrees below the MMS footprints and next to the LANL-01A footprints, despite cloudy weather (not shown) has detected auroral activations at approximately the same

time as the All-Sky Imager at The Pas. This is in agreement with the geosynchronous observations when the LANL-01A and GOES-14 satellites detected the energetic electron injections at about the same time (around 9:23 UT in Figure 2).

The global map of the ionospheric currents (Figure 8; were consistent with the plots provided by the AMPERE (not shown here)) revealed that the arc at The Pas corresponded to the ionospheric upward R2 current. For small substorms, when the azimuthal extent of the ground upward and downward currents is comparable to the latitudinal size of the substorm current system (e.g., Figure 1 in Panov et al., 2016 for a substorm with $AE \approx 120$ nT), it may be tempting to interpret the current system in terms of “current wedge” (McPherron et al., 1973), rather than attributing the upward ionospheric current to the R2 current. The present observations are in line with the predictions of the deep bubble injection simulations by Yang et al. (2012) and with the phenomenological conclusions based on statistical observations of the dipolarization development inside GEO (Ohtani et al., 2018) suggesting that DI fronts should be part of a current system that includes both R1 and R2 ionospheric currents.

Around 9:29:00 UT the azimuthal auroral arc turned into a spiral-like structure with diameter of few hundred kilometers. “Spiraling” during BBFs is not unique. A similar auroral “spiral” was observed by ASI at Ranking Inlet during flow braking on 23 March 2009 around 6:11:33 UT (Panov et al., 2014). As in the present event, the structure appeared during the expansion phase of a small (AE about 120 nT) substorm. More events showing similar “spirals” in association with BBFs (e.g., Keiling et al., 2009, where the spiral was associated with vortices in the equivalent ionospheric currents, similar to the vortices in the beginning of the substorm under study; cf. panel at 9:30 UT in Figure 8 and Figure 9 in Panov et al., 2013a) suggest generality of this phenomenon during BBF braking and rebound. Perhaps auroral spirals might be an indicator of BBF’s tailward rebounds in ASI observations.

Finally, a monochromatic Π_2 pulsations chain was observed in the magnetic field at GOES-13 (Figure 3) starting from the injection onsets at LANL-01A, GOES-15, and GOES-14. Similar-period pulsations were seen further eastward at LANL-1994-084 in the energetic electrons with energies between 200 and 750 keV. At GOES-14 similar Π_2 waves were observed after the end of the dipolarization (after about 9:30 UT). The waves were XY_{GSM} polarized. The wave period was about 90–100 s. This appeared to be 8 times smaller than the rebound time (over 12 min) implying that the wave generation cannot be explained by the buoyancy oscillations (Panov et al., 2014, 2015; Wolf et al., 2018). Since the waves were clearly related to the injection of the energetic electrons with energies between 200 and 750 keV, generation mechanisms due to resonant wave-particle interactions should be considered instead (e.g., Takahashi et al., 2018).

Acknowledgments

The authors are thankful to all of the GOES, LANL-GEO, MMS, and THEMIS teams for making their data available to the public. GOES data are available from the NOAA archival data (http://satdat.ngdc.noaa.gov/sem/goes/data/new_avg/). MMS data are available at their website (<https://lasp.colorado.edu/mms/sdc/>). THEMIS data are available at their website (<http://themis.ssl.berkeley.edu/index.shtml>). We acknowledge NASA contract NAS5-02099 for use of data from the THEMIS Mission, and specifically, for the GBO/ASIs, we acknowledge S. Mende and E. Donovan, NASA contract NAS5-02099 and the CSA for logistical support in fielding and data retrieval from the GBO stations. The work of W. B., R. N., and E. V. P. was supported by the Austrian Science Fund (FWF): I 2016-N20 and I 3506-N27. The work of M. V. K. was supported by the Russian Science Foundation (RSF) grant 18-47-05001. The authors thank J. Birn, V. G. Merkin, S. Sazykin, M. I. Sitnov, F. Toffoletto, R. A. Wolf, and J. Yang for insightful discussions.

7. Conclusions

We presented magnetotail, geosynchronous, and ionospheric observations during a substorm on 9 August 2016 between 9 and 10 UT using MMS, GOES, and LANL probes, as well as the ground magnetometer networks over Greenland and North America. We found that two broad (6.5 and 4 R_E in Y_{GSM}) DI fronts impinged and rebounded from Earth’s dipolar field lines near GEO during the same substorm. The impingements and rebounds ended with a substorm R1/R2 current system covering azimuthally the whole North American continent. The R1/R2 currents were initiated by the first DI front. The R1/R2 currents were contributed by the second DI front causing a significant local current disturbance. At the fronts, negative $j \cdot E'$ indicated negative energy dissipation. This is consistent with the Joule heating in the ionosphere at the auroral arc that was observed near the GOES-14 footprint around the time of the first DI front’s passing by the probe.

References

- Amm, O., & Kauristie, K. (2002). Ionospheric signatures of bursty bulk flows. *Surveys in Geophysics*, 23, 1–32.
- Angelopoulos, V., Coroniti, F. V., Kennel, C. F., Kivelson, M. G., Walker, R. J., Russell, C. T., et al. (1996). Multipoint analysis of a bursty bulk flow event on April 11, 1985. *Journal of Geophysical Research*, 101, 4967–4989.
- Apatenkov, S. V., Sergeev, V. A., Kubyshkina, M. V., Nakamura, R., Baumjohann, W., Runov, A., et al. (2007). Multi-spacecraft observation of plasma dipolarization/injection in the inner magnetosphere. *Annales Geophysicae*, 25, 801–814.
- Arnold, H., Swisdak, M., & Drake, J. F. (2018). Characterizing ion flows across a magnetotail dipolarization jet. *Journal of Geophysical Research: Space Physics*, 123, 6326–6334. <https://doi.org/10.1029/2018JA025604>
- Baker, D. N., Fritz, T. A., Wilken, B., Highbie, P. R., Kaye, S. M., Kivelson, M. G., et al. (1982). Observation and modeling of energetic particles at synchronous orbit on July 29, 1977. *Journal of Geophysical Research*, 87, 5917–5932.

- Baumjohann, W., Hesse, M., Kokubun, S., Mukai, T., Nagai, T., & Petrukovich, A. A. (1999). Substorm dipolarization and recovery. *Journal of Geophysical Research*, *104*, 24995–25000.
- Baumjohann, W., Paschmann, G., & Luehr, H. (1990). Characteristics of high-speed ion flows in the plasma sheet. *Journal of Geophysical Research*, *95*, 3801–3809.
- Baumjohann, W., Pellinen, R. J., Oppenoorth, H. J., & Nielsen, E. (1981). Joint two-dimensional observations of ground magnetic and ionospheric electric fields associated with auroral zone currents—Current systems associated with local auroral break-ups. *Planetary and Space Science*, *29*, 431–435.
- Belian, R. D., Gisler, G. R., Cayton, T., & Christensen, R. (1992). High-Z energetic particles at geosynchronous orbit during the great solar proton event series of October 1989. *Journal of Geophysical Research*, *97*, 16.
- Birn, J., & Hesse, M. (2014). The substorm current wedge: Further insights from MHD simulations. *Journal of Geophysical Research: Space Physics*, *119*, 3503–3513. <https://doi.org/10.1002/2014JA019863>
- Birn, J., Hesse, M., Nakamura, R., & Zaharia, S. (2013). Particle acceleration in dipolarization events. *Journal of Geophysical Research: Space Physics*, *118*, 1960–1971. <https://doi.org/10.1002/jgra.50132>
- Birn, J., Nakamura, R., Panov, E. V., & Hesse, M. (2011). Bursty bulk flows and dipolarization in MHD simulations of magnetotail reconnection. *Journal of Geophysical Research*, *116*, A01210. <https://doi.org/10.1029/2010JA016083>
- Birn, J., Thomsen, M. F., Borovsky, J. E., Reeves, G. D., McComas, D. J., Belian, R. D., & Hesse, M. (1998). Substorm electron injections: Geosynchronous observations and test particle simulations. *Journal of Geophysical Research*, *103*, 9235–9248.
- Blake, J. B., Mauk, B. H., Baker, D. N., Carranza, P., Clemmons, J. H., Craft, J., et al. (2016). The Fly's Eye Energetic Particle Spectrometer (FEEPS) sensors for the Magnetospheric Multiscale (MMS) Mission. *Space Science Reviews*, *199*, 309–329.
- Boström, R. (1964). A model of the auroral electrojets. *Journal of Geophysical Research*, *69*, 4983–4999.
- Burch, J. L., Moore, T. E., Torbert, R. B., & Giles, B. L. (2016). Magnetospheric Multiscale overview and science objectives. *Space Science Reviews*, *199*, 5–21.
- Chen, C. X. (2016). Substorm onset: A switch on the sequence of transport from decreasing entropy to increasing entropy. *Geophysical Research Letters*, *43*, 4834–4840. <https://doi.org/10.1002/2016GL069114>
- Chen, C. X., & Wolf, R. A. (1999). Theory of thin-filament motion in Earth's magnetotail and its application to bursty bulk flows. *Journal of Geophysical Research*, *104*, 14613–14626.
- Cowley, S. W. H. (2000). TUTORIAL: Magnetosphere-ionosphere interactions: A tutorial review. *Washington DC American Geophysical Union Geophysical Monograph Series*, *118*, 91. <https://doi.org/10.1029/GM118p0091>
- Dubyagin, S., Sergeev, V., Apatenkov, S., Angelopoulos, V., Runov, A., Nakamura, R., et al. (2011). Can flow bursts penetrate into the inner magnetosphere? *Geophysical Research Letters*, *38*, L08102. <https://doi.org/10.1029/2011GL047016>
- Gabrielse, C., Angelopoulos, V., Runov, A., & Turner, D. L. (2014). Statistical characteristics of particle injections throughout the equatorial magnetotail. *Journal of Geophysical Research: Space Physics*, *119*, 2512–2535. <https://doi.org/10.1002/2013JA019638>
- Gkioulidou, M., Ohtani, S., Mitchell, D. G., Ukhorskiy, A. Y., Reeves, G. D., Turner, D. L., et al. (2015). Spatial structure and temporal evolution of energetic particle injections in the inner magnetosphere during the 14 July 2013 substorm event. *Journal of Geophysical Research: Space Physics*, *120*, 1924–1938. <https://doi.org/10.1002/2014JA020872>
- Goldstein, J., Burch, J. L., Sandel, B. R., Mende, S. B., Cson Brandt, P., & Hairston, M. R. (2005). Coupled response of the inner magnetosphere and ionosphere on 17 April 2002. *Journal of Geophysical Research*, *110*, A03205. <https://doi.org/10.1029/2004JA010712>
- Hanser, F. A. (2011). EPS/HEPAD calibration and data handbook. Assurance Technology Corporation, Carlisle, Mass. Available at <http://www.ngdc.noaa.gov/stp/satellite/goes/documentation.html>
- Keiling, A., Angelopoulos, V., Weygand, J. M., Amm, O., Spanswick, E., Donovan, E., et al. (2009). THEMIS ground-space observations during the development of auroral spirals. *Annales Geophysicae*, *27*, 4317–4332. <https://doi.org/10.5194/angeo-27-4317-2009>
- Kubyskhina, M., Sergeev, V., Tsyganenko, N., Angelopoulos, V., Runov, A., Donovan, E., et al. (2011). Time-dependent magnetospheric configuration and breakup mapping during a substorm. *Journal of Geophysical Research*, *116*, A00127. <https://doi.org/10.1029/2010JA015882>
- Li, X., Baker, D. N., Temerin, M., Reeves, G. D., & Belian, R. D. (1998). Simulation of dispersionless injections and drift echoes of energetic electrons associated with substorms. *Geophysical Research Letters*, *25*, 3763–3766.
- Liu, J., Angelopoulos, V., Chu, X., Zhou, X.-Z., & Yue, C. (2015a). Substorm current wedge composition by wedgelets. *Geophysical Research Letters*, *42*, 1669–1676. <https://doi.org/10.1002/2015GL063289>
- Liu, J., Angelopoulos, V., Zhou, X.-Z., Yao, Z.-H., & Runov, A. (2015b). Cross-tail expansion of dipolarizing flux bundles. *Journal of Geophysical Research: Space Physics*, *120*, 2516–2530. <https://doi.org/10.1002/2015JA020997>
- Lopez, R. E., Sibeck, D. G., McEntire, R. W., & Krimigis, S. M. (1990). The energetic ion substorm injection boundary. *Journal of Geophysical Research*, *95*, 109–117.
- Lui, A. T. Y. (1996). Current disruption in the Earth's magnetosphere: Observations and models. *Journal of Geophysical Research*, *101*, 13067–13088.
- Lui, A. T. Y. (2004). Potential plasma instabilities for substorm expansion onsets. *Space Science Reviews*, *113*, 127–206.
- Lui, A. T. Y., & Kamide, Y. (2003). A fresh perspective of the substorm current system and its dynamo. *Geophysical Research Letters*, *30*(18), 1958. <https://doi.org/10.1029/2003GL017835>
- Malykhin, A. Y., Grigorenko, E. E., Kronberg, E. A., Koleva, R., Ganushkina, N. Y., Kozak, L., & Daly, P. W. (2018). Contrasting dynamics of electrons and protons in the near-Earth plasma sheet during dipolarization. *Annales Geophysicae*, *36*, 741–760.
- Mann, I. R., Milling, D. K., Rae, I. J., Ozeke, L. G., Kale, A., Kale, Z. C., et al. (2008). The upgraded CARISMA magnetometer array in the THEMIS era. *Space Science Reviews*, *141*, 413–451.
- Mauk, B. H., & McIlwain, C. E. (1974). Correlation of kp with the substorm-injected plasma boundary. *Journal of Geophysical Research*, *79*, 3193–3196.
- McPherron, R. L., Nakamura, R., Kokubun, S., Kamide, Y., Shiokawa, K., Yumoto, K., et al. (1997). Fields and flows at GEOTAIL during a moderate substorm. *Advances in Space Research*, *20*, 923–931.
- McPherron, R. L., Russell, C. T., & Aubry, M. P. (1973). Satellite studies of magnetospheric substorms on August 15, 1968: 9. Phenomenological model for substorms. *Journal of Geophysical Research*, *78*, 3131.
- Mende, S. B., Harris, S. E., Frey, H. U., Angelopoulos, V., Russell, C. T., Donovan, E., et al. (2008). The THEMIS Array of Ground-based Observatories for the Study of Auroral Substorms. *Space Science Reviews*, *141*, 357–387.
- Miyashita, Y., Angelopoulos, V., Fukui, K., & Machida, S. (2018). A case study of near-earth magnetotail conditions at substorm and pseudosubstorm onsets. *Geophysical Research Letters*, *45*, 6353–6361. <https://doi.org/10.1029/2018GL078589>
- Moore, T. E., Arnoldy, R. L., Feynman, J., & Hardy, D. A. (1981). Propagating substorm injection fronts. *Journal of Geophysical Research*, *86*, 6713–6726.

- Moore, T. E., Chandler, M. O., Buzulukova, N., Collinson, G. A., Kepko, E. L., Garcia-Sage, K. S., et al. (2013). "Snowplow" injection front effects. *Journal of Geophysical Research: Space Physics*, *118*, 6478–6488. <https://doi.org/10.1002/jgra.50573>
- Nakamura, R., Baker, D. N., Yamamoto, T., Belian, R. D., Bering, E. A., Benbrook, J. R., & Theall, J. R. (1994). Particle and field signatures during pseudobreakup and major expansion onset. *Journal of Geophysical Research*, *99*, 207–221.
- Nakamura, R., Baumjohann, W., Mouikis, C., Kistler, L. M., Runov, A., Volwerk, M., et al. (2004). Spatial scale of high-speed flows in the plasma sheet observed by Cluster. *Geophysical Research Letters*, *31*, L09804. <https://doi.org/10.1029/2004GL019558>
- Nakamura, R., Baumjohann, W., Panov, E., Volwerk, M., Birn, J., Artemyev, A., et al. (2013). Flow bouncing and electron injection observed by Cluster. *Journal of Geophysical Research: Space Physics*, *118*, 2055–2072. <https://doi.org/10.1002/jgra.50134>
- Nakamura, R., Baumjohann, W., Schödel, R., Brittnacher, M., Sergeev, V. A., Kubyshkina, M., et al. (2001). Earthward flow bursts, auroral streamers, and small expansions. *Journal of Geophysical Research*, *106*, 10791–10802.
- Ohtani, S.-i. (1998). Earthward expansion of tail current disruption: Dual-satellite study. *Journal of Geophysical Research*, *103*, 6815–6826.
- Ohtani, S., Motoba, T., Gkioulidou, M., Takahashi, K., & Singer, H. J. (2018). Spatial development of the dipolarization region in the inner magnetosphere. *Journal of Geophysical Research: Space Physics*, *123*, 5452–5463. <https://doi.org/10.1029/2018JA025443>
- Ohtani, S., Singer, H. J., & Mukai, T. (2006). Effects of the fast plasma sheet flow on the geosynchronous magnetic configuration: Geotail and GOES coordinated study. *Journal of Geophysical Research*, *111*, A01204. <https://doi.org/10.1029/2005JA011383>
- Palin, L., Opgenoorth, H. J., Ågren, K., Zivkovic, T., Sergeev, V. A., Kubyshkina, M. V., et al. (2016). Modulation of the substorm current wedge by bursty bulk flows: 8 September 2002—Revisited. *Journal of Geophysical Research: Space Physics*, *121*, 4466–4482. <https://doi.org/10.1002/2015JA022262>
- Panov, E. V., Artemyev, A. V., Baumjohann, W., Nakamura, R., & Angelopoulos, V. (2013). Transient electron precipitation during oscillatory BBF braking: THEMIS observations and theoretical estimates. *Journal of Geophysical Research: Space Physics*, *118*, 3065–3076. <https://doi.org/10.1002/jgra.50203>
- Panov, E. V., Baumjohann, W., Kubyshkina, M. V., Nakamura, R., Sergeev, V. A., Angelopoulos, V., et al. (2014). On the increasing oscillation period of flows at the tailward retreating flux pileup region during dipolarization. *Journal of Geophysical Research: Space Physics*, *119*, 6603–6611. <https://doi.org/10.1002/2014JA020322>
- Panov, E. V., Baumjohann, W., Nakamura, R., Amm, O., Kubyshkina, M. V., Glassmeier, K.-H., et al. (2013a). Ionospheric response to oscillatory flow braking in the magnetotail. *Journal of Geophysical Research: Space Physics*, *118*, 1529–1544. <https://doi.org/10.1002/jgra.50190>
- Panov, E. V., Baumjohann, W., Nakamura, R., Kubyshkina, M. V., Glassmeier, K.-H., Angelopoulos, V., et al. (2014). Period and damping factor of Pi2 pulsations during oscillatory flow braking in the magnetotail. *Journal of Geophysical Research: Space Physics*, *119*, 4512–4520. <https://doi.org/10.1002/2013JA019633>
- Panov, E. V., Baumjohann, W., Wolf, R. A., Nakamura, R., Angelopoulos, V., Weyand, J. M., & Kubyshkina, M. V. (2016). Magnetotail energy dissipation during an auroral substorm. *Nature Physics*, *12*, 1158–1163. <https://doi.org/10.1038/nphys3879>
- Panov, E. V., Kubyshkina, M. V., Nakamura, R., Baumjohann, W., Angelopoulos, V., Sergeev, V. A., & Petrukovich, A. A. (2013b). Oscillatory flow braking in the magnetotail: THEMIS statistics. *Geophysical Research Letters*, *40*, 2505–2510. <https://doi.org/10.1002/grl.50407>
- Panov, E. V., Nakamura, R., Baumjohann, W., Angelopoulos, V., Petrukovich, A. A., Retinó, A., et al. (2010). Multiple overshoot and rebound of a bursty bulk flow. *Geophysical Research Letters*, *37*, L08103. <https://doi.org/10.1029/2009GL041971>
- Panov, E. V., Nakamura, R., Baumjohann, W., Sergeev, V. A., Angelopoulos, V., Petrukovich, A. A., et al. (2010). Plasma sheet thickness during a bursty bulk flow reversal. *Journal of Geophysical Research*, *115*, A05213. <https://doi.org/10.1029/2009JA014743>
- Panov, E. V., Wolf, R. A., Kubyshkina, M. V., Nakamura, R., & Baumjohann, W. (2015). Anharmonic oscillatory flow braking in the Earth's magnetotail. *Geophysical Research Letters*, *42*, 3700–3706. <https://doi.org/10.1002/2015GL064057>
- Pollock, C., Moore, T., Jacques, A., Burch, J., Gliese, U., Saito, Y., et al. (2016). Fast plasma investigation for Magnetospheric Multiscale. *Space Science Reviews*, *199*, 331–406.
- Reeves, G. D., Belian, R. D., & Fritz, T. A. (1991). Numerical tracing of energetic particle drifts in a model magnetosphere. *Journal of Geophysical Research*, *96*, 13.
- Reeves, G. D., Belian, R. D., & Fritz, T. A. (1996). Radial propagation of substorm injections. In *Proceedings of the 3rd International Conference on Substorms, Versailles, France, 12-17 May 1996*, pp. 579–584.
- Reeves, G. D., Fritz, T. A., Cayton, T. E., & Belian, R. D. (1990). Multi-satellite measurements of the substorm injection region. *Geophysical Research Letters*, *17*, 2015–2018.
- Runov, A., Angelopoulos, V., Sitnov, M. I., Sergeev, V. A., Bonnell, J., McFadden, J. P., et al. (2009). THEMIS observations of an earthward-propagating dipolarization front. *Geophysical Research Letters*, *36*, L14106. <https://doi.org/10.1029/2009GL038980>
- Sergeev, V., Angelopoulos, V., Apatenkov, S., Bonnell, J., Ergun, R., Nakamura, R., et al. (2009). Kinetic structure of the sharp injection/dipolarization front in the flow-braking region. *Geophysical Research Letters*, *36*, L21105. <https://doi.org/10.1029/2009GL040658>
- Sergeev, V. A., Angelopoulos, V., Gosling, J. T., Cattell, C. A., & Russell, C. T. (1996). Detection of localized, plasma-depleted flux tubes or bubbles in the midtail plasma sheet. *Journal of Geophysical Research*, *101*, 10817–10826.
- Sergeev, V. A., Chernyaev, I. A., Angelopoulos, V., Runov, A. V., & Nakamura, R. (2014). Stopping flow bursts and their role in the generation of the substorm current wedge. *Geophysical Research Letters*, *41*, 1106–1112. <https://doi.org/10.1002/2014GL059309>
- Sergeev, V. A., Chernyaev, I. A., Dubyagin, S. V., Miyashita, Y., Angelopoulos, V., Boakes, P. D., et al. (2012). Energetic particle injections to geostationary orbit: Relationship to flow bursts and magnetospheric state. *Journal of Geophysical Research*, *117*, A10207. <https://doi.org/10.1029/2012JA017773>
- Sergeev, V. A., Sauvaud, J.-A., Popescu, D., Kovrazhkin, R. A., Liou, K., Newell, P. T., et al. (2000). Multiple-spacecraft observation of a narrow transient plasma jet in the Earth's plasma sheet. *Geophysical Research Letters*, *27*, 851–854.
- Sergeev, V. A., Shukhtina, M. A., Rasinkangas, R., Korth, A., Reeves, G. D., Singer, H. J., et al. (1998). Event study of deep energetic particle injections during substorm. *Journal of Geophysical Research*, *103*, 9217–9234.
- Siscoe, G. L. (1982). Energy coupling between regions 1 and 2 Birkeland current systems. *Journal of Geophysical Research*, *87*, 5124–5130.
- Strangeway, R. J. (2012). The equivalence of Joule dissipation and frictional heating in the collisional ionosphere. *Journal of Geophysical Research*, *117*, A02310. <https://doi.org/10.1029/2011JA017302>
- Sugiura, M. (1975). Identifications of the polar cap boundary and the auroral belt in the high-altitude magnetosphere—A model for field-aligned currents. *Journal of Geophysical Research*, *80*, 2057–2068.
- Takahashi, K., Hartinger, M. D., Vellante, M., Heilig, B., Lysak, R. L., Lee, D.-H., & Smith, C. W. (2018). Roles of flow braking, plasmaspheric virtual resonances, and ionospheric currents in producing ground Pi2 pulsations. *Journal of Geophysical Research: Space Physics*, *123*, 9187–9203. <https://doi.org/10.1029/2018JA025664>
- Thomsen, M. F., Birn, J., Borovsky, J. E., Morzinski, K., McComas, D. J., & Reeves, G. D. (2001). Two-satellite observations of substorm injections at geosynchronous orbit. *Journal of Geophysical Research*, *106*, 8405–8416.

- Torbert, R. B., Russell, C. T., Magnes, W., Ergun, R. E., Lindqvist, P.-A., Le Contel, O., et al. (2016). The FIELDS instrument suite on MMS: Scientific objectives, measurements, and data products. *Space Science Reviews*, *199*, 105–135.
- Turner, D. L., Claudepierre, S. G., Fennell, J. F., O'Brien, T. P., Blake, J. B., Lemon, C., et al. (2015). Energetic electron injections deep into the inner magnetosphere associated with substorm activity. *Geophysical Research Letters*, *42*, 2079–2087. <https://doi.org/10.1002/2015GL063225>
- Ukhorskiy, A. Y., Sorathia, K. A., Merkin, V. G., Sitnov, M. I., Mitchell, D. G., & Gkioulidou, M. (2018). Ion trapping and acceleration at dipolarization fronts: High-resolution MHD and test-particle simulations. *Journal of Geophysical Research: Space Physics*, *123*, 5580–5589. <https://doi.org/10.1029/2018JA025370>
- Untiedt, J., & Baumjohann, W. (1993). Studies of polar current systems using the IMS Scandinavian magnetometer array. *Space Science Reviews*, *63*, 245–390.
- Weygand, J. M., Amm, O., Viljanen, A., Angelopoulos, V., Murr, D., Engebretson, M. J., et al. (2011). Application and validation of the spherical elementary currents systems technique for deriving ionospheric equivalent currents with the North American and Greenland ground magnetometer arrays. *Journal of Geophysical Research*, *116*, A03305. <https://doi.org/10.1029/2010JA016177>
- Wolf, R. A., Chen, C. X., & Toffoletto, F. R. (2012). Thin filament simulations for Earth's plasma sheet: Interchange oscillations. *Journal of Geophysical Research*, *117*, A02215. <https://doi.org/10.1029/2011JA016971>
- Wolf, R. A., Kumar, V., Toffoletto, F. R., Erickson, G. M., Savoie, A. M., Chen, C. X., & Lemon, C. L. (2006). Estimating local plasma sheet $PV^{5/3}$ from single-spacecraft measurements. *Journal of Geophysical Research*, *111*, A12218. <https://doi.org/10.1029/2006JA012010>
- Wolf, R. A., Toffoletto, F. R., Schutza, A. M., & Yang, J. (2018). Buoyancy waves in Earth's magnetosphere: Calculations for a 2d wedge magnetosphere. *Journal of Geophysical Research: Space Physics*, *123*, 3548–3564. <https://doi.org/10.1029/2017JA025006>
- Yang, J., Toffoletto, F. R., Wolf, R. A., & Sazykin, S. (2011). RCM-E simulation of ion acceleration during an idealized plasma sheet bubble injection. *Journal of Geophysical Research*, *116*, A05207. <https://doi.org/10.1029/2010JA016346>
- Yang, J., Toffoletto, F. R., Wolf, R. A., Sazykin, S., Ontiveros, P. A., & Weygand, J. M. (2012). Large-scale current systems and ground magnetic disturbance during deep substorm injections. *Journal of Geophysical Research*, *117*, A04223. <https://doi.org/10.1029/2011JA017415>